Quasi-Static Monotonic and Cyclic Tests on Composite Spandrels

Katrin Beyer,[a), c)] M.EERI, **and Alessandro Dazio,**[b), c)] M.EERI

In modern unreinforced masonry (URM) walls, the vertical piers are connected at the story levels by reinforced concrete (RC) ring beams—also known as bond beams—or RC slabs. Particularly, in the outer walls, the spandrel element also includes a masonry spandrel on top of the RC beam or slab ("composite" spandrel). Numerical simulations have shown that spandrels significantly influence the global behavior of the URM building when subjected to seismic loading. Despite their importance, experimental data on the cyclic behavior of composite spandrels were lacking. This paper presents the results of an experimental campaign on five composite spandrels. Each test unit consisted of an RC beam, a masonry spandrel and the adjacent masonry piers required for applying realistic boundary conditions to the spandrel. The investigated parameters included the type of loading, the brick type and the reinforcement content of the RC beam. [DOI: 10.1193/1.4000058]

INTRODUCTION

Horizontal spandrel elements can contribute significantly to the global stiffness and resistance of unreinforced masonry (URM) structures (e.g., Magenes and Della Fontana 1998, Magenes 2000, Milani et al. 2009). This holds in particular for URM buildings with reinforced concrete (RC) slabs or ring beams; in the United States the latter are also often referred to as bond beams. Nevertheless, most design approaches neglect the framing action due to the horizontal spandrel elements and consider only the vertical piers when calculating the strength and stiffness of the URM wall. The main reason for neglecting the spandrels is the lack of experimental data for the behavior of spandrels under seismic loading because spandrel elements with RC beams or slabs have yet been tested. For this reason, an experimental campaign was performed at the ETH Zurich, Switzerland, in which spandrel elements were tested under quasi-static monotonic and cyclic loading. The experimental program was divided into two parts. In one part, spandrels typical for modern URM buildings with RC ring beams or RC slabs were tested. In the second part, spandrels typical for old masonry buildings were tested. These spandrels included either a wooden lintel and a masonry spandrel or a masonry spandrel with a shallow arch to bridge the opening. The major differences between the two parts of the test program concern (i) the presence or absence of a reinforced concrete (RC) beam in the first and second part, respectively, and (ii) the brick type. This paper presents the experimental campaign on spandrels with RC beams.

[a)] Ecole Polytechnique Fédérale de Lausanne (EPFL), 1015 Lausanne, Switzerland
[b)] EUCENTRE, 27100 Pavia, Italy
[c)] Formerly Eidgenössische Technische Hochschule Zürich (ETHZ), 8093 Zürich, Switzerland

Earthquake Spectra, Volume 28, No. 3, pages 885–906, August 2012; © 2012, Earthquake Engineering Research Institute

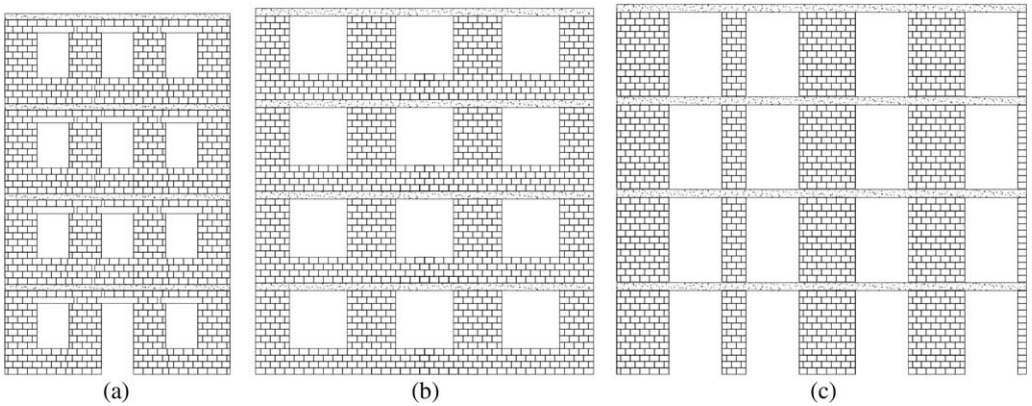

Figure 1. Facades of masonry buildings with RC slabs and different spandrel types: Spandrels consisting (a) of masonry spandrel, RC slab and lintel, (b) of masonry spandrel and RC slab, and (c) of an RC slab only.

Facades of buildings with RC slabs feature three different types of spandrels. The first type of spandrel consists of a masonry spandrel, a strip of the RC slab and an RC or reinforced masonry lintel (Figure 1a). This type of spandrel is typically found in older buildings with RC slabs. Larger window openings are indicative of newer construction. Often, the lintel disappears altogether and the window frame with the roller shutter casing reach up to the RC slab (Figure 1b). In very recent buildings, even the masonry spandrel above the slab sometimes disappears and the window unit reaches over the entire story height (Figure 1c). In these cases, the coupling of the masonry piers results from the RC slab only. A similar coupling mechanism can be found in the inner walls where the coupling action due to the RC slab is sometimes reinforced by a door lintel. In view of the large variety of spandrel elements in modern URM buildings, it is impossible to conduct large-scale tests on all types of spandrels. The tests will serve only for the validation of numerical models. For this reason it was decided to concentrate on spandrel elements which comprise a masonry spandrels and a strip of a RC slab. Once the numerical model will be validated, a much larger range of spandrel configurations will be analyzed and then tested. The following sections present the test units, the test setup and the most important test results.

TEST UNITS

Five composite spandrels were tested, and the test units were labeled as "TU1" through "TU5." All test units had the same geometry and consisted of an RC beam, a masonry spandrel and a masonry pier on either side of the spandrel (Figure 2). The masonry piers were required for applying the load to the spandrel element. The parameters investigated included (i) the type of brick, (ii) the loading regime and (iii) the longitudinal reinforcement content of the RC beams. Two of the spandrels were subjected to monotonic loading (TU1 and TU2) and three to cyclic loading (TU3-TU5, Table 1). TU1 and TU2 differed concerning the type of masonry that was used. For the construction of TU1, bricks with staggered longitudinal webs and a mortar with a high tensile strength were used. TU2-TU5 spandrels were

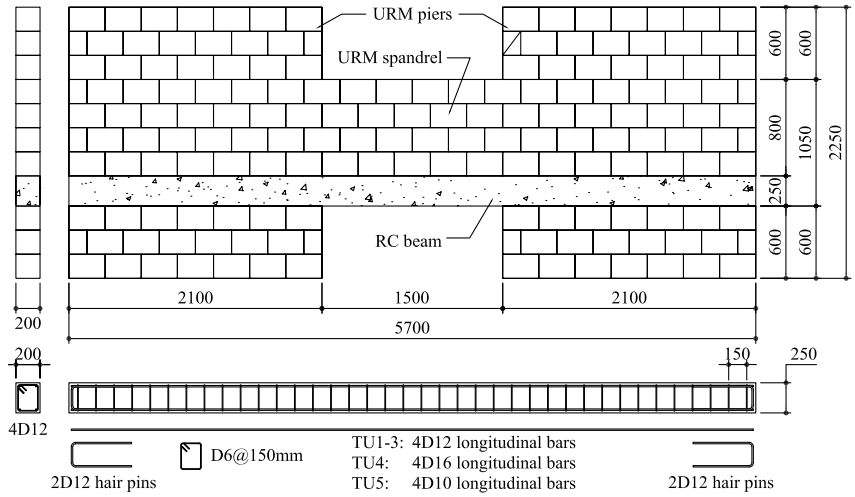

Figure 2. Geometry of test unit and reinforcing layout of RC beam.

Table 1. Loading scheme, reinforcement content of the RC beams and details of the axial load application and the brick types for the five test units.

Test Unit	Loading	Longit. reinf. of RC beam	Shear reinf. of RC beam	Axial stress in piers	Brick dimensions and type
TU1	Monotonic	4 D12 mm ($4.52\ cm^2$)	D6 s = 150 mm	0.4 MPa	290 × 200 × 190 mm, Staggered webs
TU2	Monotonic	4 D12 mm ($4.52\ cm^2$)	D6 s = 150 mm	0.4 MPa	290 × 200 × 190 mm, Continuous webs
TU3	Cyclic	4 D12 mm ($4.52\ cm^2$)	D6 s = 150 mm	0.4 MPa	290 × 200 × 190 mm, Continuous webs
TU4	Cyclic	4 D16 mm ($8.04\ cm^2$)	D6 s = 150 mm	0.4 MPa (0.6 MPa[1)])	290 × 200 × 190 mm, Continuous webs
TU5	Cyclic	4 D10 mm ($3.14\ cm^2$)	D6 s = 150 mm	0.4 MPa	290 × 200 × 190 mm, Continuous webs

[1)]Axial stress in piers was increased for the final cycles.

constructed using bricks with continuous longitudinal webs and a mortar with a lower tensile strength; the latter being one of the most commonly used mortars for masonry construction in Switzerland. Since it has not yet been shown that the force-deformation relationships of spandrel elements obtained from a monotonic test corresponds well to the envelope of a cyclic test, two identical test units were subjected to the two different loading regimes: TU2 (monotonic loading) and TU3 (cyclic loading). The final two test units were also subjected to cyclic loading but the longitudinal reinforcement content of the RC beams was varied. The RC beams of TU1-3 had a longitudinal reinforcement of 4 D12 mm bars. The RC beam of

Table 2. Mechanical properties of the concrete (mean values and standard deviations).

Test unit	$f_{c,cube}$ [MPa]	f_c [MPa]	E_{cm} [GPa]	f_{ct} [1)] [MPa]	f_{ct} [2)] [MPa]
TU1+TU3	39.2±1.6	35.2±1.6	31.0±1.8	3.38±0.32	6.20±0.16
TU2	37.8±1.1	33.4±1.6	30.0±0.4	3.36	6.49
TU4	35.6±1.1	30.2±0.8	27.8±0.6	2.79	5.39
TU5	36.7±1.4	31.4±0.5	29.1±1.0	2.62	7.04

[1)]Tensile strength obtained from double punch tests (Chen 1970) on a cylinder with a diameter of 150 mm and a height of 150 mm.
[2)]Tensile strength obtained from three-point bending tests of prisms (120×120×360 mm) according to CEN (2009b).

TU4 had a longitudinal reinforcement that was almost twice as large (4 D16 mm), satisfying the minimum requirements for RC ring beams according to the Italian seismic design code OPCM (2005). Only the shear reinforcement of D6 mm hoops every 150 mm was stronger than the required D6 mm hoops every 250 mm. According to the European seismic design code EC 8 (CEN 2005), a ring beam must be fitted with a minimum longitudinal reinforcement area of 2 cm^2, which is considerably smaller than the reinforcement area of TU1-TU4. For this reason, a fifth beam was tested with a smaller longitudinal reinforcement area (TU5: 4 D10 mm). Note that EC 8 makes no specifications concerning the minimum shear reinforcement content.

MATERIAL PROPERTIES OF TEST UNITS

The spandrel tests were complemented by a material test program on reinforcing bars, concrete, mortar, brick and masonry properties. All material tests were performed near the time when the spandrels were tested; thus, the measured quantities reflect the material strengths at the time of the spandrel tests. Details on testing dates, specimen preparation, the testing procedure and evaluation of the material tests are given in Beyer et al. (2010a).

Table 2 gives the cube strength $f_{c,cube}$ (CEN 2009a), the cylinder strength f_c (CEN 2009a), the E-modulus E_{cm} (SIA 2003a), and the tensile strength f_{ct} (CEN 2009b, Chen 1970) for the concrete. The properties of the reinforcing bars, expressed in terms of static and dynamic yield and ultimate strength ($f_{y,stat}$, $f_{t,stat}$, $f_{y,dyn}$, and $f_{t,dyn}$), were determined from monotonic tensile tests in displacement control (CEN, 2006b) and are summarized in Table 3. All stress values are based on the nominal area of the bar. The deformation capacity of the bars is described by means of A_{gt}, which is the total elongation at maximum force.

All bricks had nominal dimensions of 290×200×190 mm ($L \times T \times H$). With head and bed joints of 10 mm, the layout of the masonry was 300×200×200 mm. Table 4 summarizes the geometric and mechanical properties of the bricks. The compressive strength (CEN 2000) and E-Modulus for loading in the vertical direction ($f_{cb,x}$ and $E_{b,x}$) and the longitudinal direction of the brick ($f_{cb,y}$ and $E_{b,y}$) were determined from compression tests on single bricks (Figure 3a and b). To estimate the tensile strength of the bricks, three-point bending tests were performed on specimens consisting of three bricks (Figure 3c). The three bricks

Table 3. Mechanical properties of the reinforcing bars (mean values and standard deviations).

	D6	D10	D12	D16
$f_{y,dyn}$ [MPa]	586±14.3	535±1.9	540±13.6	505±2.6
$f_{t,dyn}$ [MPa]	634±13.0	646±2.3	630±3.7	616±2.2
$f_{t,dyn}/f_{y,dyn}$	1.08±0.01	1.21±0.01	1.17±0.02	1.22±0.01
$f_{y,stat}$ [MPa]	563±13.6	510±4.4	501±10.5	485±6.1
$f_{t,stat}$ [MPa]	596±17.3	618±2.9	576±2.9	581±4.9
$f_{t,stat}/f_{y,stat}$	1.06±0.01	1.21±0.02	1.15±0.02	1.20±0.02
A_{gt} [%]	4.9±0.36	8.7±0.59	6.8±0.69	12.8±0.58

Table 4. Mechanical properties of Type 1 and Type 2 bricks (mean values and standard deviations).

Brick Type / Property	Type 1 (TU1)	Type 2 (TU2-5)	Ratio Type 2 / 1
Ratio area of holes / gross area	42%	36%	0.86
Width of cont. webs in longit. (y) dir. [mm]	23	76	3.30
Width of cont. webs in transv. (z) dir. [mm]	92	106	1.15
$f_{cb,x}$ [MPa]	24.7±3.2	30.9±3.1	1.25
$E_{b,x}$ [GPa]	8.4±1.2	14.0±3.8	1.91
$f_{cb,y}$ [MPa]	3.5±0.2	8.9±1.2	2.58
$E_{b,y}$ [GPa]	2.1±0.5	6.1±1.9	2.87
f_{tb} [MPa]	0.7±0.0	1.4±0.3	1.92

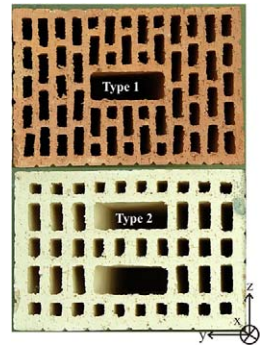

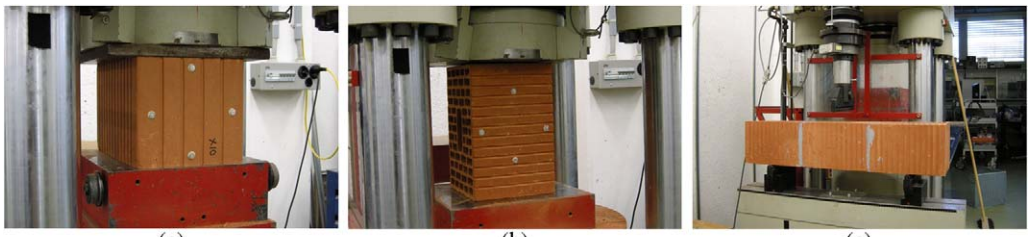

Figure 3. Material tests on bricks: (a) Compression test in the vertical (x) direction, (b) compression test in the longitudinal (y) direction, and (c) three-point bending test with a clear span of 600 mm.

were glued together at their head faces using an epoxy-based adhesive. Tensile failure occurred in the middle brick. The tensile strength, f_{tb}, was computed as the maximum bending moment divided by the section modulus W of the middle brick and by assuming gross sectional properties, that is, $W = bh^2/6$.

A different brick type was used for TU1 than for TU2-5. The main difference between the two brick types is the layout of the webs along the longitudinal direction of the bricks. The photos in Table 4 show that the inner webs of Brick Type 1 were staggered while for Brick Type 2 all the inner webs were continuous. The formation of the inner webs had a particularly strong influence on the compressive strength in the longitudinal direction ($f_{cb,y}$) and on the flexural strength (Table 4).

A different type of mortar (Kelit 110) was used for TU1 than for the construction of the other test units (Maxitmur 920). Both mortars are Portland cement-based. They are delivered in sacks and are frequently used for bearing and nonbearing standard brickworks in Switzerland. To determine the tensile strength, f_{ctm}, and the compressive strength, f_{cm}, of the mortar, mortar prisms (40×40×160 mm) were sampled at regular intervals during the construction of the test units (CEN 2006a). Three-point bending tests with a free span of 100 mm and cube compression tests were performed (Table 5).

To determine the shear characteristics of the joints, standard tests on masonry triplets at different normal stresses were performed (CEN 2007). Only triplets with Brick Type 2 were tested. The mortar used for the construction of the triplets was a Maxitmur 920 mortar with a compression strength of $f_{cm} = 10.8$ MPa on the day of testing. The peak shear stresses can be described by the Mohr-Coulomb relationship: $\tau_{max} = 0.71\sigma + 0.25$ ($R^2 = 0.78$). The residual shear stresses is best captured by the equation $\tau_{res} = 0.70\sigma + 0.03$ ($R^2 = 0.97$) but similarly well by the following equation with a friction term only: $\tau_{res} = 0.77\sigma$ ($R^2 = 0.96$).

To determine the stiffness and strength of the masonry, tests on small masonry wallettes were performed (Figure 4). The compression tests were conducted orthogonal (x-direction; CEN 2002) and parallel (y-direction; SIA 2003b) to the bed joints. The resulting strengths (f_{mx} and f_{my}) and E-moduli (E_{mx} and E_{my}) are summarized in Table 5. TU2 and TU3 as well as TU4 and TU5 were constructed pairwise simultaneously. For each construction phase only one group of masonry wallettes consisting of six masonry wallettes each was constructed. For this reason the masonry properties of TU2/TU3 and TU4/TU5 were equal.

Table 5. Mechanical properties of mortar and masonry (mean values and standard deviations).

Test unit	f_{cm} [MPa]	f_{ctm} [MPa]	f_{mx} [MPa]	E_{mx} [GPa]	f_{my} [MPa]	E_{my} [GPa]
TU1	16.5±3.2	4.6±0.3	6.6	8.5	1.3±0.0	2.9±0.3
TU2+TU3	11.4±2.3	2.5±0.7	4.0±0.5	5.3±1.0	1.3±0.2	1.8±0.6
TU4	12.2±0.9	3.2±0.3	6.4±0.5	7.0±1.2	1.4±0.2	1.2±0.4
TU5	12.1±0.9	2.9±0.2	6.4±0.5	7.0±1.2	1.4±0.2	1.2±0.4

Figure 4. Material tests on masonry wallettes: Masonry wallettes representing TU1 (a) test in x-direction and (b) test in y-direction; and masonry wallettes representing TU2 and TU3 (c) test in x-direction, and (d) test in y-direction.

TEST SETUP, INSTRUMENTATION AND LOADING HISTORY

TEST SETUP

In the test setup, the test unit stood on two stiff beams ("lever beams") that were supported on hinges at the center line of the piers and connected to servo-hydraulic actuators at their ends (Figures 5 and 6). During testing, the two servo-hydraulic actuators were moved

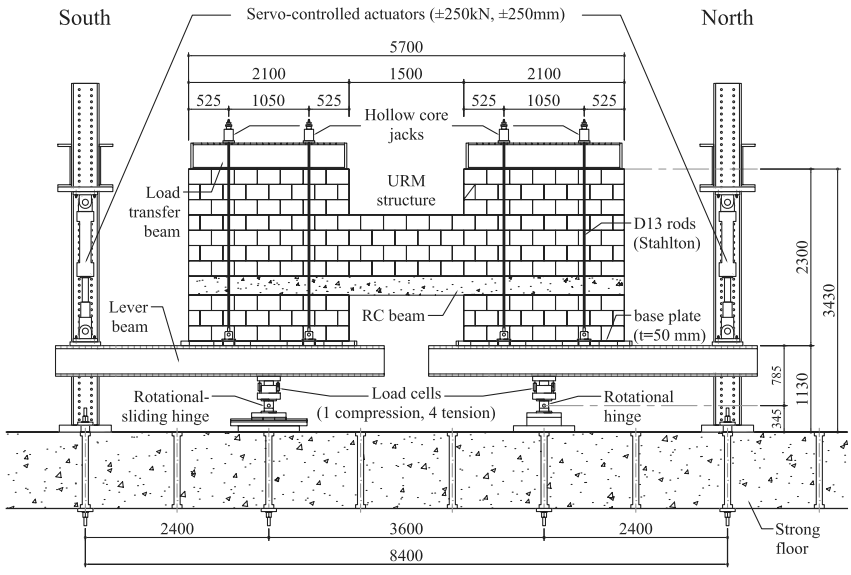

Figure 5. Drawing of the test setup for the composite spandrel: view from the east without side restraint. All dimensions are in mm.

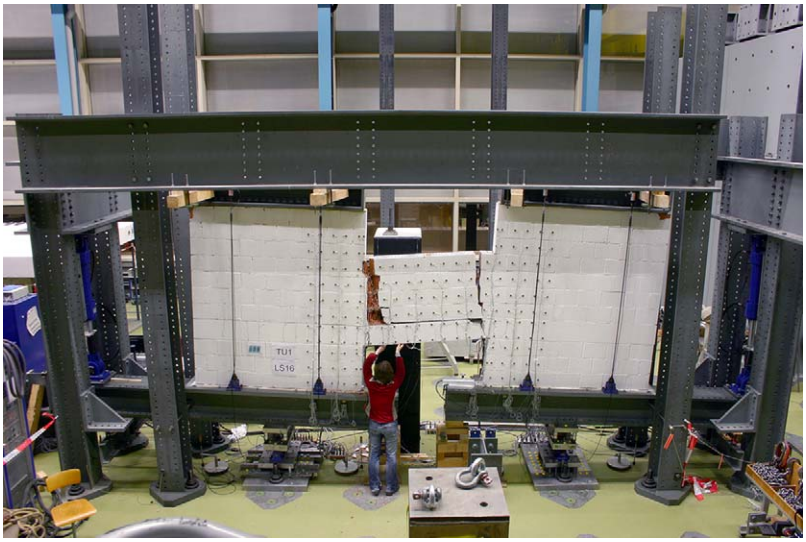

Figure 6. Photo of the test setup: View from the east.

with the same velocity in opposite directions. As a result, the two horizontal lever beams rotated and the piers right and left to the spandrel were subjected to the same drifts, which caused the demand on the spandrel. The support of the South lever beam allowed the rotation of the lever beam and also a sliding movement along the longitudinal axis of the beam. Hence, the test stand did not restrain the axial elongation of the spandrel. The two piers were post-tensioned by four vertical rods each. The forces in the vertical rods were kept constant throughout the test although, in reality, the axial force in piers varies due to framing action and vertical accelerations.

The test setup differs from the test setup used at the University of Trieste (Gattesco et al. 2008) and at the University of Pavia (Graziotti et al. 2009) for the testing of masonry spandrels. In a numerical study before the test campaign, the authors of this paper investigated several different test setups; among these, the test setup that was eventually adopted by the Italian research groups. Both test setups were able to reproduce the demand on the spandrel encountered in an URM building. The authors' preference of the test setup, shown in Figure 5, was related to concerns involving the control of the servo-hydraulic actuators. Because the weight of the test unit was supported on the rotational hinges underneath the lever beams, a possible loss of pressure in the servo-hydraulic system causes less damage to the test unit than the previously published test setup. The test setup worked very reliably throughout all tests.

INSTRUMENTATION

Different global and local quantities were measured during testing by means of hard-wired instruments (Figure 7). The most important global deformation quantity was the rotation of the piers, which was computed from the LVDTs mounted underneath the

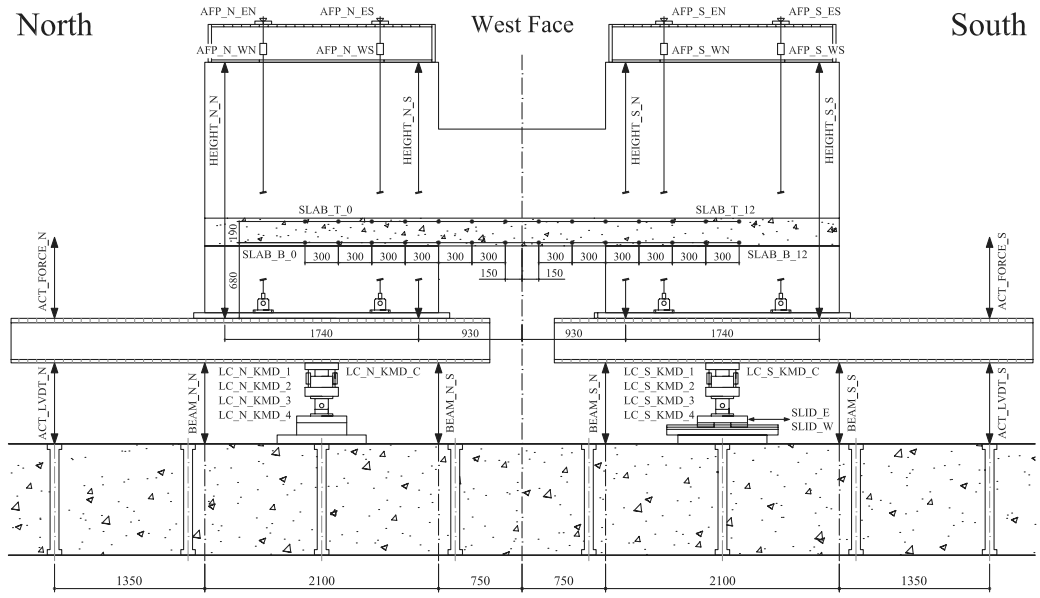

Figure 7. Layout of the hard-wired instruments for composite spandrels: View from the west. All dimensions in mm.

lever beams. The final drift was computed as the average rotation of the North and South lever beams:

$$\theta = (\theta_N + \theta_S)/2 \tag{1}$$

The demand on the spandrel does not only depend on the pier rotations but also on the length of the spandrel. A "spandrel displacement" was computed as (Milani et al. 2009):

$$\Delta_{sp} = \theta \cdot (l_{sp} + l_{pier}) \tag{2}$$

where l_{sp} is the length of the spandrel and l_{pier} is the length of the pier. For the tested spandrels, these lengths were 1.50 m and 2.10 m, respectively. From the measurements of the actuator forces and the forces at the supports, the shear force in the spandrel was computed.

LOADING HISTORY

Both the monotonic and cyclic loading scheme followed different steps of story drifts in displacement control. The drift is defined as positive when the piers are displaced toward the North (Figure 8). When the monotonic loading scheme was applied, loading was stopped at the following nominal drift levels (Figure 9a): θ_{nom}: 0.025%, 0.05%, 0.1%, 0.2%, 0.3%, 0.4%, 0.6%, 0.8%, 1.0%, 1.5%, 2.0%, 2.5%, and 3.0%. The same drift levels determined the amplitudes of the cyclic loading scheme (Figure 9b). At each drift level, the test unit was subjected to two cycles. The nominal drift refers to the target drift of a load step.

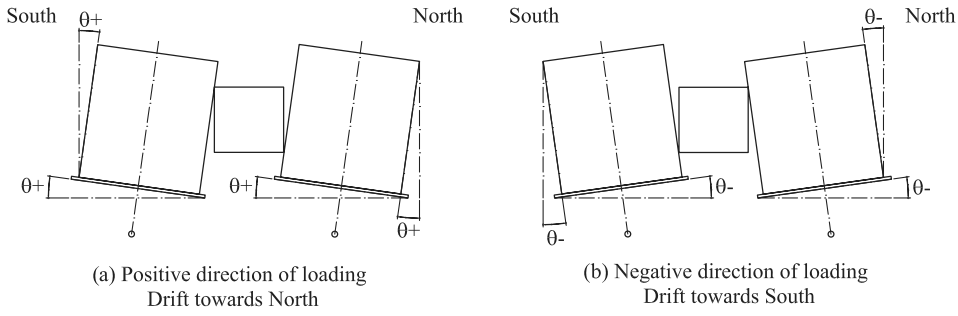

Figure 8. (a) Positive and (b) negative direction of loading: View from the east.

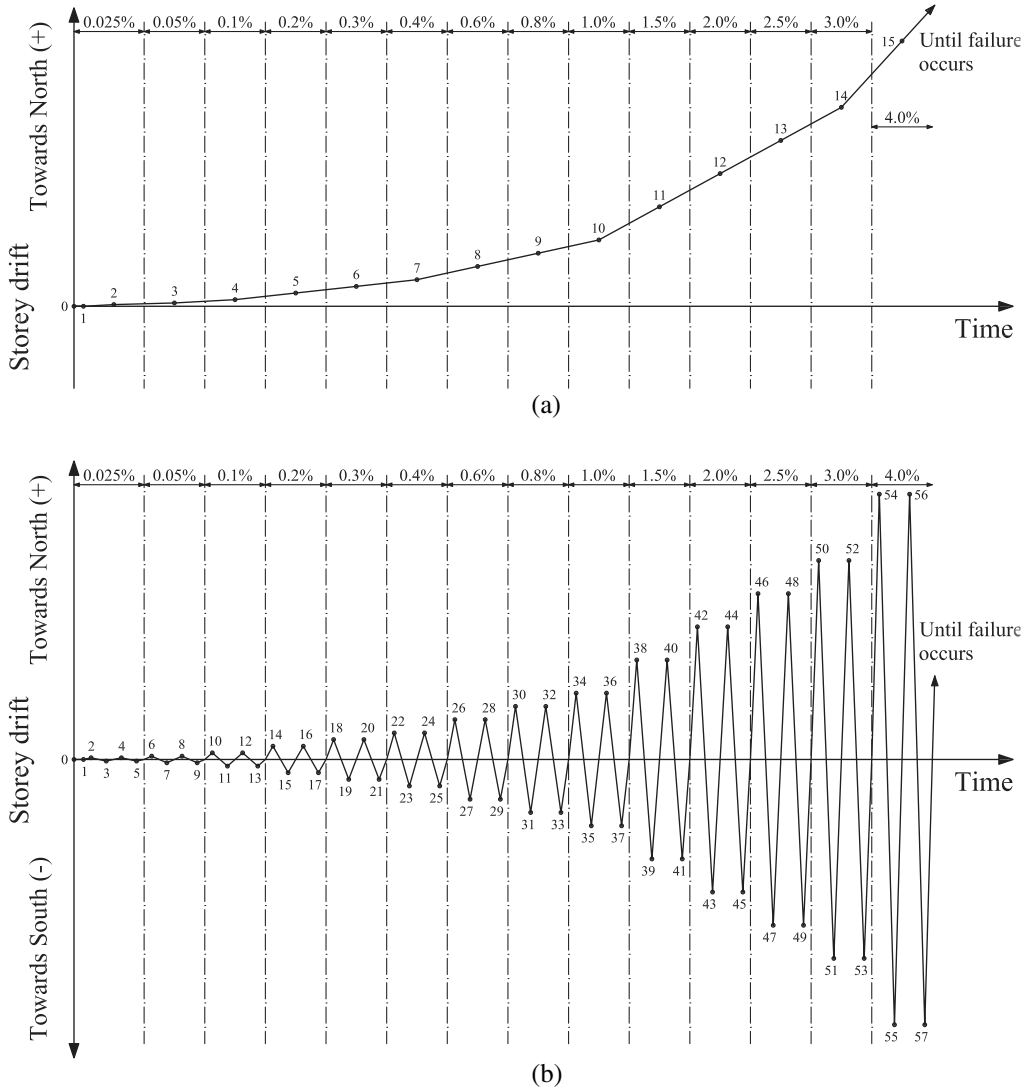

Figure 9. Loading history for (a) the monotonic and (b) the cyclic loading schemes.

The numbering of the drift-controlled load steps commences with LS 2. LS 0 refers to the state before any rotations or forces were applied, and LS 1 refers to the state when the axial load was applied to the piers.

TEST RESULTS

In the following section, selected test results of the two monotonic and three cyclic tests are presented that characterize the global behavior of the spandrels. In the first section, the general development of the crack pattern and the failure mechanisms are summarized. In the second section, the force-deformation curves are compared and discussed.

TEST OBSERVATIONS

The general behavior of a composite spandrel observed for a positive rotation demand on the piers is depicted in Figure 10. For small longitudinal reinforcement ratios of the RC beam (TU5), a compression diagonal reached from the South end of the spandrel into the spandrel (Figure 10a). The compression diagonal was supported by the RC beam, which was subjected to positive bending at this position. Hence, the positive plastic hinge in the RC beam formed not at the South end of the spandrel, as one would conclude if the masonry spandrel was neglected, but within the span of the spandrel. The negative plastic hinge in the RC beam, on the contrary, formed at the North end of the spandrel. Further differences between the two plastic hinges concerned their length: while the North (negative) plastic hinge was rather short, the South (positive) plastic hinge was typically spread over a longer part of the RC beam. The plastic hinges also differed with regard to the type of cracks that formed: the cracks of the positive plastic hinge were mainly flexural cracks, while some of the cracks of the negative plastic hinge were inclined shear-flexural cracks. For large longitudinal reinforcement ratios (TU4), the RC beam was so strong that for the initial level of vertical prestress in the pier ($\sigma = 0.4$ MPa), a positive plastic hinge did not form in the RC beam. Instead, the beam rocked on the pier, that is, a gap between pier and the bottom of the RC beam opened up almost over the entire length of the pier (Figure 10b). From previous tests on masonry piers, it is known that such a rocking mechanism has a very large deformation capacity (Frumento et al. 2009). For intermediate longitudinal reinforcement ratios (TU1-TU3), the mechanism that formed was a combination of the two mechanisms depicted in Figure 10, that is, the gap between RC beam and pier opened up to some extent, but the positive plastic hinge in the RC beam still formed.

This general description of the mechanisms applied to all five test units for small to medium rotation demands and it agrees well with numerical results on spandrels and URM walls

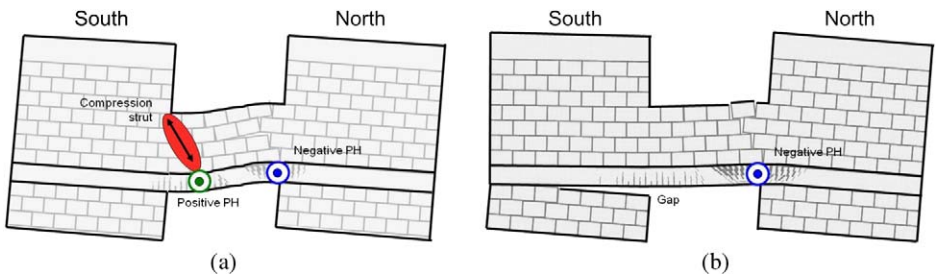

Figure 10. Mechanical models based on the observed crack pattern: (a) Mechanism with two plastic hinges in RC beam and (b) rocking mechanism with a negative plastic hinge only.

with RC slabs, which were performed before the experimental tests (Beyer et al. 2010b). In the following section, the development of the crack pattern and the failure mechanism of the five test units are outlined and compared.

Out of the five composite spandrels, TU1 showed a very different crack pattern than the others: vertical cracks at both ends of the spandrel extended over the entire height of the spandrel and ran almost straight through the bricks (Figure 11). Up to failure, the body of the masonry spandrel remained virtually undamaged and all the deformation demand

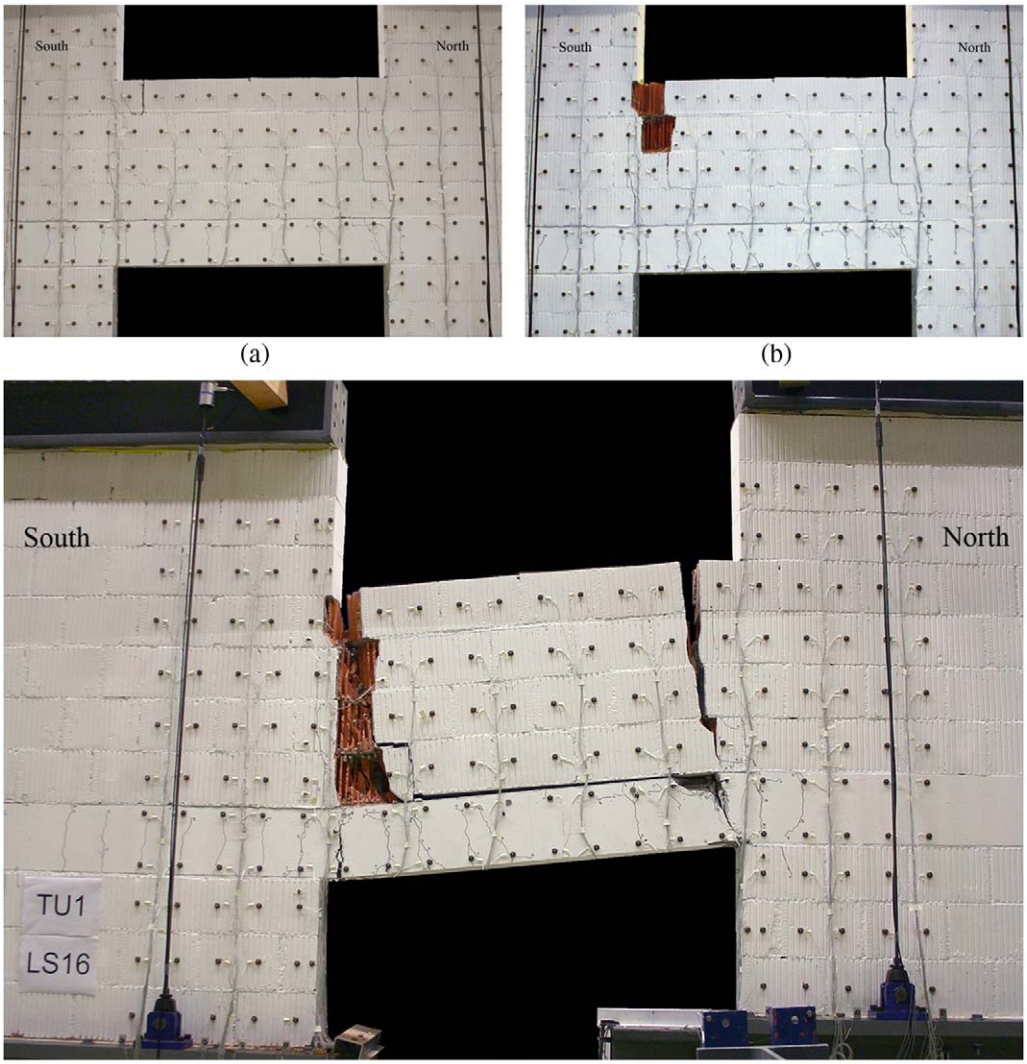

Figure 11. TU1: Crack pattern at (a) LS 7 ($\theta_{nom} = +0.4\%$), (b) LS 9 ($\theta_{nom} = 0.8\%$), and (b) LS 16 (failure of TU1 at $\theta = +5.3\%$, c).

on the masonry spandrel was absorbed by the two flexural cracks. At the South end of the spandrel, the compression strut reaching into the spandrel (the spandrel was subjected to monotonic loading toward the North only) caused crushing of the bricks. Crushing commenced in the top rows of the spandrel (Figure 11b). Due to the crushing, the compression diagonal moved to the South and thus leading to crushing of the bricks located below the top row. Eventually, a vertical column about half a brick wide failed (Figure 11c). Very early during the test the masonry spandrel separated from the RC beam beneath it. Plastic hinges formed at both ends of the beam, leading eventually to failure due to the rupture of longitudinal reinforcing bars. The difference in the behavior of TU1 from the other composite test units was caused by the strong anisotropy of the masonry due to the staggered webs, which weakened the bricks particularly in the horizontal direction (see Table 1).

The first cracks in TU2 appeared when loading to LS 4 ($\theta_{nom} = +0.4\%$). At this load step, two stair-stepped cracks had formed in the masonry and one crack in each of the regions of the RC beam that were to become the positive and negative plastic hinges. At $\theta_{nom} = +0.4\%$ (LS 7, Figure 12a) and $\theta_{nom} = +0.8\%$ (Figure 12b) the spandrel was subjected to significant cracking but had not yet passed its peak strength. A drift of $\theta = 0.4\%$ corresponds to the ultimate limit state pier drifts assumed in EC 8 (CEN 2005) for shear failure; a drift of $\theta = 0.8\%$ corresponds to the ultimate limit state drift for a pier failing in flexure and a height of zero moment to pier length ratio equal to one. The final crack pattern of the masonry spandrel of TU2 at failure was characterized by two major stair-stepped cracks (Figure 12c). At the beginning of the test, the bricks of TU2 remained largely undamaged and the cracks followed the joints. As the deformation demand increased, crushing of the compression diagonal occurred, leading to a Southward shift of the positive plastic hinge. The final failure of the test unit was caused by the rupture of longitudinal bars in both the negative and the positive plastic hinges.

TU3 was the first test unit subjected to cyclic loading. Similar to TU2, the first cracks appeared during the cycles with $\theta_{nom} = +0.1\%$. At $\theta_{nom} = \pm 0.4\%$, the crack pattern was almost completely developed and further cracks indicated mainly the crushing of the compression diagonals in the masonry spandrel. Figures 13a and b show the crack pattern at LS 30 and LS 31, which corresponded to the first positive and negative peaks of the cycles with amplitude $\theta_{nom} = \pm 0.8\%$, respectively. The photos show that although the spandrel was almost completely cracked, the deformation behavior for the two directions of loading was not exactly the same: For the positive direction of loading, the bulk deformation of the spandrel concentrated in one large crack. However, for the negative direction of loading, the deformation was distributed over two parallel cracks. As loading continued, the crushing of the compression diagonals became stronger. When compared to the monotonic loading, it appeared that all bricks were disjointed and the deformations accumulated in crack widths more equally distributed over the spandrel. For the RC beam, the cyclic behavior led to a larger growth in the length of the RC beam because the plastic strain in the longitudinal reinforcing bars had accumulated. As a consequence, at the same drift demand, the crack widths in the RC beam were larger for TU3 than for TU2. The shear reinforcement in the RC beam was not sufficient to carry the entire shear force of the beam. As the contribution of the concrete to the shear capacity decreased below a certain limit, a shear failure occurred within the positive plastic hinge during the first cycle with $\theta = \pm 3\%$. When the loading was reversed thereafter, also a longitudinal bar fractured within the positive plastic hinge (Figure 13c).

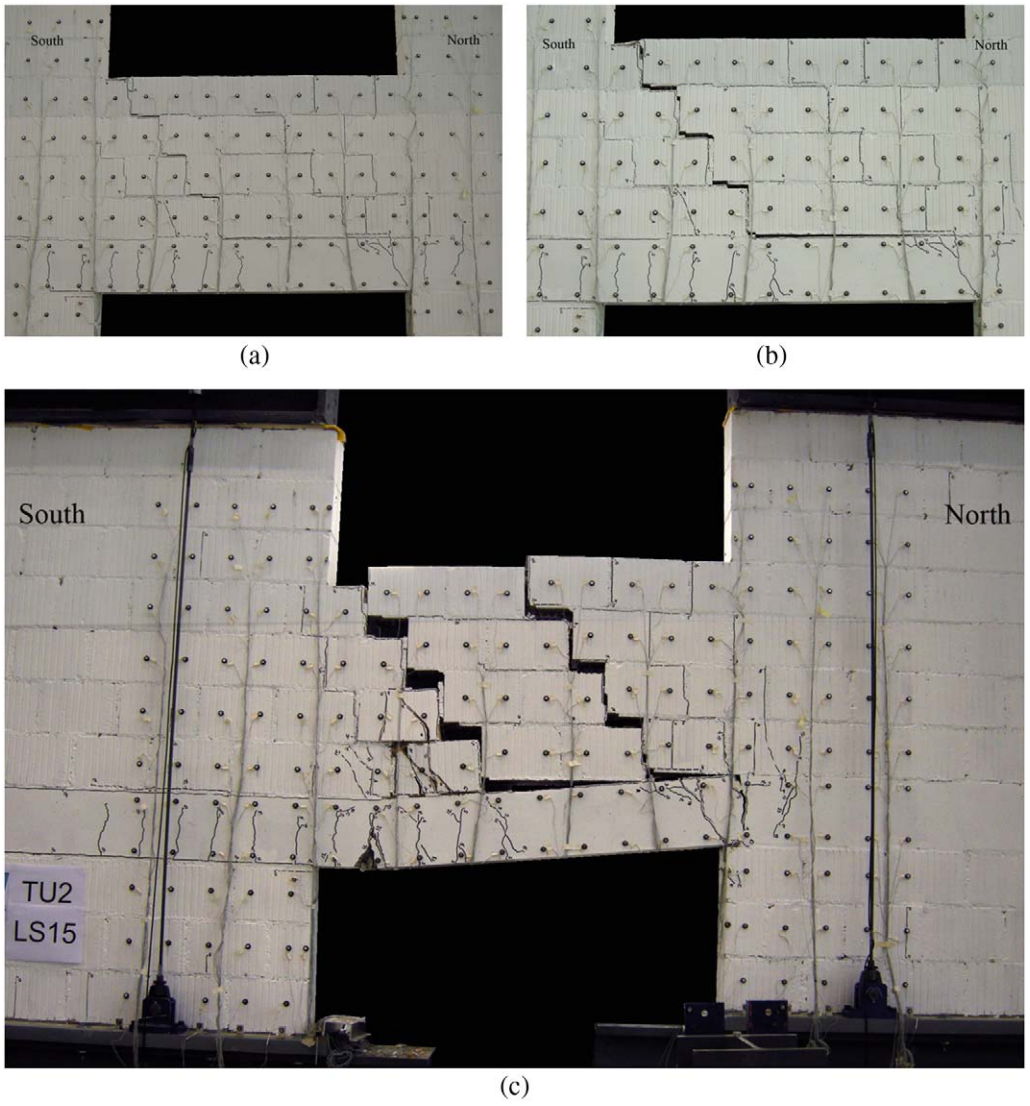

Figure 12. TU2: Crack pattern at (a) LS 7 ($\theta_{nom} = +0.4\%$), (b) LS 9 ($\theta_{nom} = +0.8\%$), and (c) LS 16 (failure of TU2 at $\theta = +4.0\%$).

The RC beam of TU4 was considerably stiffer and stronger than that of TU3 and forced a gap to open up between the bottom of the RC beam and the pier, which reduced the deformation demand on the RC beam itself (Figure 10b). For loading in the positive direction (drift toward the North) the gap opened in the South pier and only a negative plastic hinge formed in the RC beam at the location of the North end of the spandrel. No positive hinge formed in the RC beam. For loading in the negative direction (drift toward the South), the behavior was mirrored (Figure 14a). At the end of the cycles with a rotation of $\theta_{nom} = \pm 2.0\%$, the axial

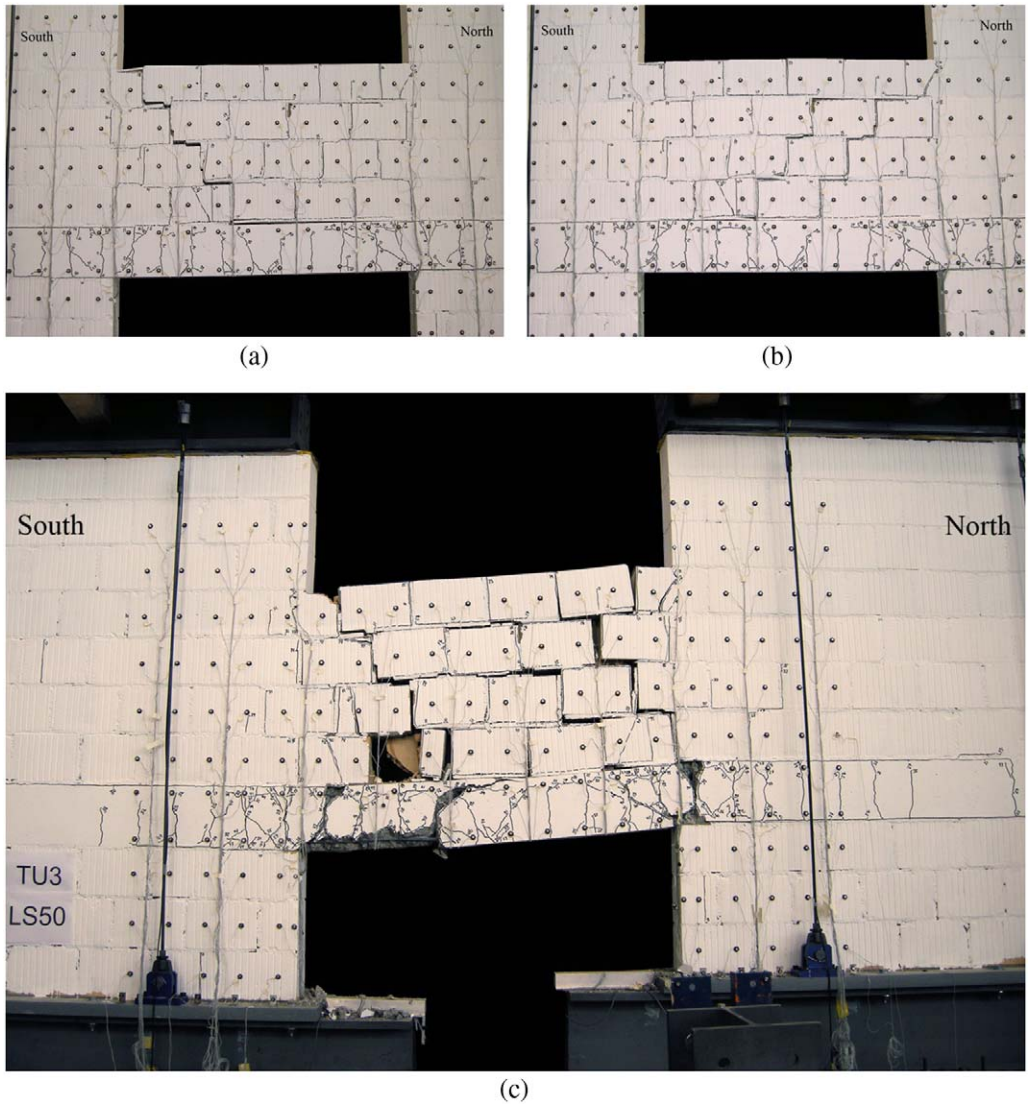

Figure 13. TU3: Crack pattern at (a) LS 30 ($\theta_{nom} = +0.8\%$), (b) LS 31 ($\theta_{nom} = -0.8\%$), and (c) LS 50 (failure of TU3 at $\theta = +3.0\%$).

stress in the piers was increased from 0.4 MPa to 0.6 MPa. Consequently, the gap between the pier and RC beam did not open up as much and the RC beam had to deform more. This increased deformation demand on the RC beam led to the yielding of the positive plastic hinge, producing shear failure of the RC beam in the second cycle (Figure 14b).

The RC beam of TU5 had a weaker longitudinal reinforcement than the first four test units. For TU5, the horizontal joint between the pier and RC beam hardly opened up and

(a)

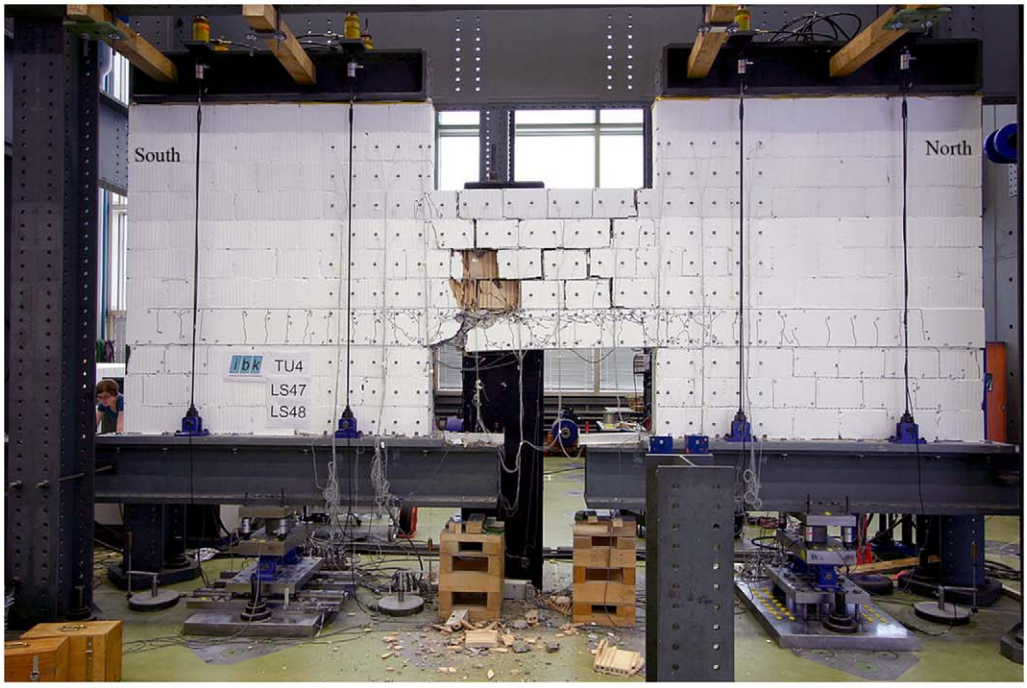

(b)

Figure 14. TU4: Crack pattern at (a) LS 45 ($\theta_{nom} = +0.8\%$) and (b) LS 50 (failure of TU4 at $\theta = +3.0$).

therefore the developing mechanism corresponded to that shown in Figure 10a. Because the longitudinal reinforcement was smaller but the shear reinforcement ratio was the same as that for TU3, the shear demand on the RC beam was less for TU5 than for TU3. As a consequence, only very few inclined shear cracks (Figure 15a) developed in the RC beam. Due to the smaller flexural strength and stiffness of the RC beam, the extent of cracking of the RC beam into the piers was also reduced. The test unit failed due to rupture of the longitudinal reinforcement (flexural failure, Figure 15b and c). However, toward the end of the test, shear

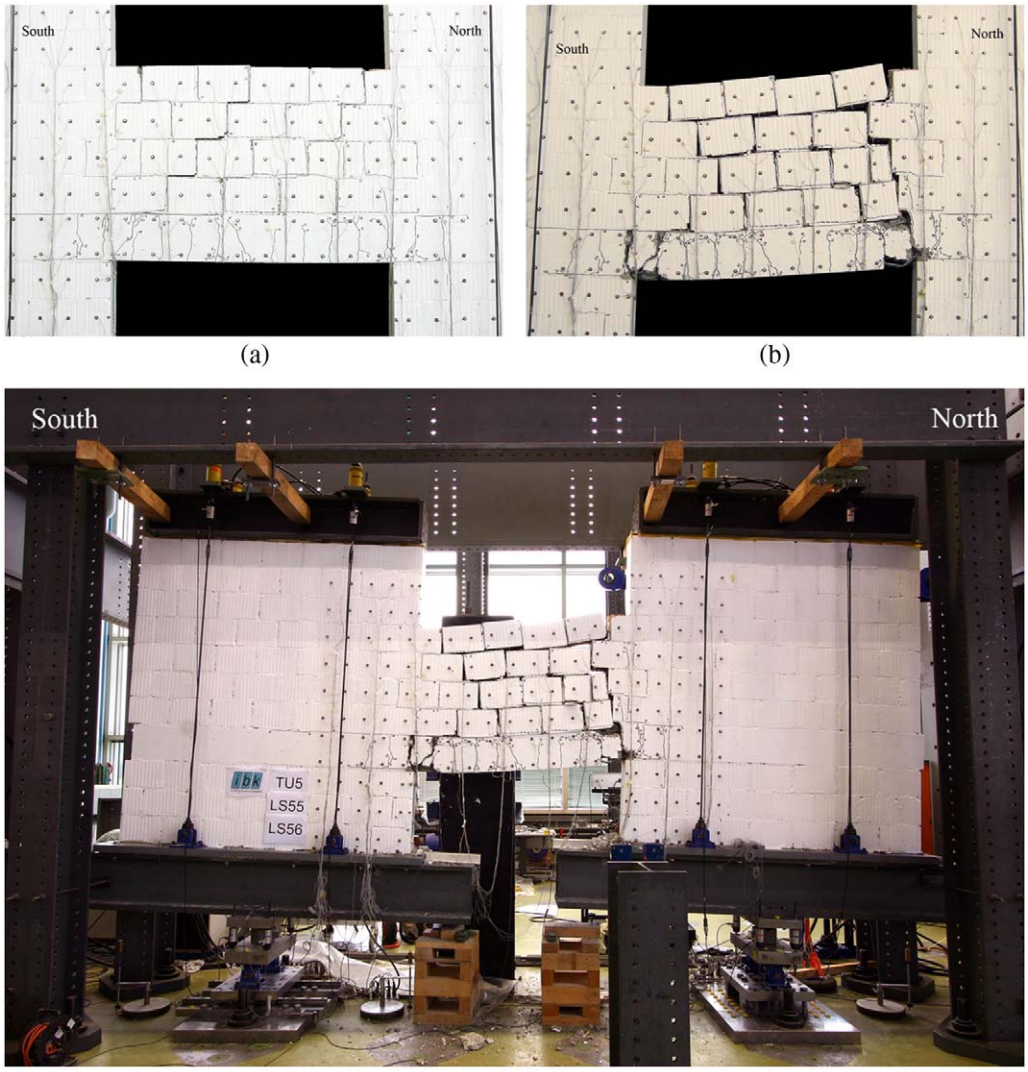

Figure 15. TU5: Crack pattern at (a) LS 31 ($\theta_{nom} = -0.8\%$), (b) LS 56 ($\theta_{nom} = +4.0\%$), and (c) LS 56 (failure of TU5 at $\theta = +4.0\%$).

transfer in the RC beam became critical; in the South negative plastic hinge, a shear crack opened up significantly. This crack did not cross a stirrup and therefore all the shear force had to be transmitted via aggregate interlock and dowel action.

HYSTERETIC BEHAVIOR

Figure 16 shows the force-rotation relationships for the spandrels from the five tests. Also included in each plot is the nominal spandrel capacity, V_{RC}, which is computed considering only the contribution of the RC beam:

$$V_{RC} = \frac{2M_n}{l_{sp}}, \tag{3}$$

where M_n is the nominal moment capacity of the RC beam and l_{sp} is the free span of the spandrel ($l_{sp} = 1.5$ m). The nominal moment capacity was obtained from a moment-curvature analysis of the RC section using the program *Response2000* (Bentz 2001) as the moment for which the maximum reinforcement strain was 1.5% or the maximum concrete

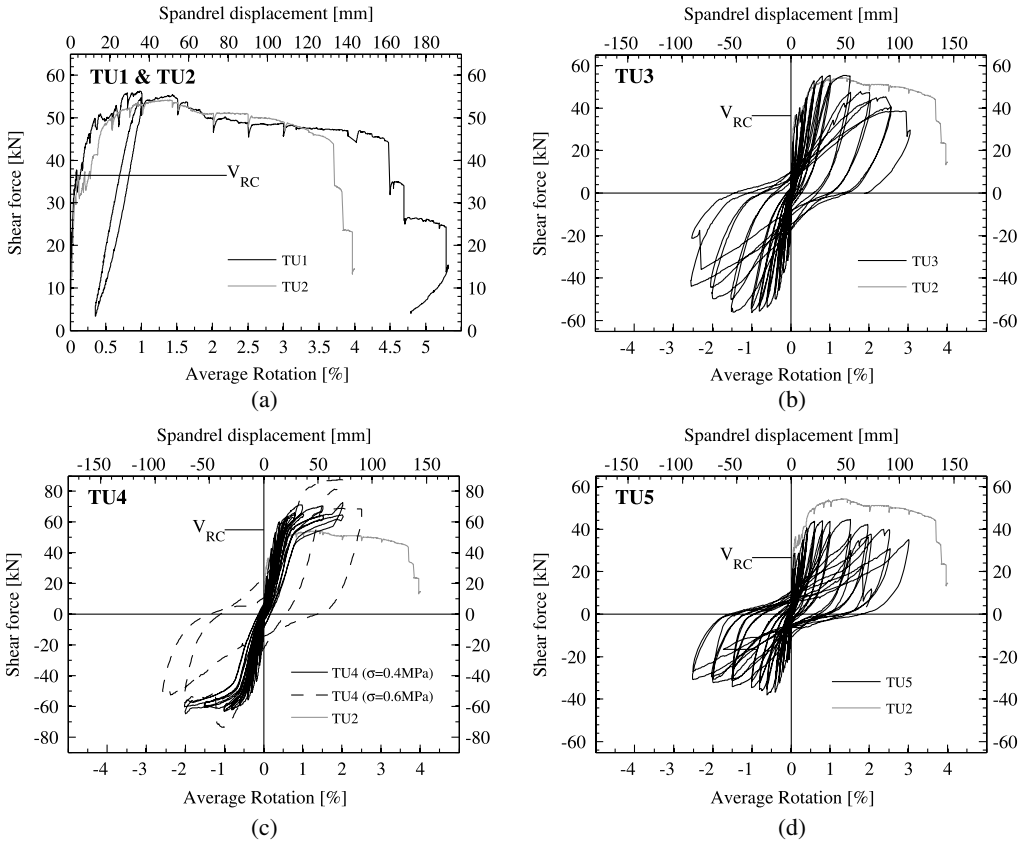

Figure 16. Force-deformation hysteresis for the test units TU1–TU5.

strain was 0.2%, whichever occurred first (Priestley et al. 2007). For TU1-TU3, TU4, and TU5 V_{RC} amounted to 36.5 kN, 54.9 kN, and 26.5 kN, respectively. For all five test units, the ratio of V_{RC} to the maximum shear force measured during the test was between 0.59–0.67. Hence, at peak strength, the masonry contributed approximately one third to the resistance of the spandrel by reducing the effective span through the inclined compression diagonal and possibly also by vertical friction forces transmitted through the spandrel.

Although TU1 and TU2 had different masonry properties and exhibited different masonry behaviors, the force-rotation relationships of TU1 and TU2 were very similar (Figure 16a). For both test units, the initial elastic phase was followed by a jagged branch, which was associated with the formation of cracks in the masonry spandrel and the RC beam. The onset of yielding in the longitudinal reinforcement of the RC beam caused the force-rotation curve to round off. It stayed level for a small range of rotations and then began to drop. This reduction in capacity starting at a rotation of 1% to 1.5% was associated with the crushing of the compression diagonal.

TU3, which was the first test unit subjected to the cyclic loading scheme, showed a very stable cyclic behavior up to a drift of 1.5% (Figure 16b). Afterward, the capacity of the test unit decreased. This reduction in capacity was again associated with the crushing of the compression diagonals in the masonry spandrel. On the whole, the envelope of TU3 corresponded very well to the force-deformation relationship of TU2, which had identical properties but had been subjected to monotonic loading. The peak capacities of TU3 exceeded even the curve of TU2 up to a drift of 1.5%, which was most likely due to the slightly higher mortar strength of TU3. TU2 and TU3 were built at the same time. Because TU2 was tested first, the mortar strength on the day of testing was slightly less than the mortar strength of TU3 on the day of testing. For drift demands larger than 1.5%, the reduction in capacity was stronger for TU3 than for TU2—most likely due to a faster degradation of the compression strut owing to the cyclic loading.

The force-deformation hysteresis of TU4 differed significantly from that of TU3. During the cycles with $\sigma = 0.4$ MPa, the hysteresis loops were almost bilinear elastic (Figure 16c) due to the rocking of the RC beam on the piers according to the mechanism described in the previous section. When the axial stress in the piers was increased to $\sigma = 0.6$ MPa, the maximum shear force in the spandrel increased and the longitudinal reinforcement of the RC beam yielded leading to fatter hysteresis loops.

The RC beam of TU5 had the smallest longitudinal reinforcement (4 D10 mm) of all the test units. It is therefore likely that the stresses in the compression diagonal of the spandrel were smaller and the crushing of the masonry played only a minor role. As a consequence, the drop in the capacity after the peak was reached was less significant (Figure 16d). It is also likely that the relative contribution of the masonry spandrel to the resistance of the spandrel element might therefore have been larger leading to the more pinched behavior of the hysteresis curves with stiffnesses recovering at the end of the cycle, which is typical for a behavior dominated by shear.

The deformation capacity of all test units was considerably larger than the drift limits that are normally assumed for failure of URM piers. As stated before, EC 8 (CEN 2005) proposes, as ultimate limit state limits for pier drifts, 0.4% and around 0.8% for shear and flexural failure, respectively. These limits correspond to the performance state “significant damage.”

The drift limits associated with "near collapse" are assumed as 33% larger (CEN 2005). At these codified pier drift capacities, the spandrels still possessed their entire force capacity. The ultimate deformation capacity of the spandrels corresponded to pier drifts between 2.5% and 4.5%, that is, drifts much larger than are typically of interest for URM buildings.

CONCLUSIONS

The five tests on spandrel test units with RC beams and masonry spandrels ("composite spandrels") showed that the masonry of the spandrel affects the load-bearing mechanism of the spandrel by reducing the effective span of the RC beam. Neglecting the masonry spandrel therefore underestimates the capacity of the spandrel element as well as the shear demand on the RC beam. A shear failure of the RC beam must be avoided in order to guarantee a stable force-displacement hysteresis of the spandrel element. For this reason, the shorter shear span due to the masonry spandrel should be considered when designing the shear reinforcement of the RC ring beam. The experiments also demonstrated that the deformation capacity of the spandrel elements is quite large and considerably exceeds for typical spandrel configurations the design story drifts of piers (CEN 2005).

The five tests on composite spandrels provide a data basis for the development of numerical and simple mechanical models for estimating the force-displacement characteristics of such spandrel elements. These activities, which are currently underway, will provide the basis for the improvement of current force-based design approaches and new displacement-based design approaches.

ACKNOWLEDGMENTS

Funding for this work was provided by the KGV Prevention Foundation in the framework of the research project "Nonlinear deformation behavior of unreinforced masonry structures through testing and numerical simulations." The tests were performed in the laboratory of the Institute of Structural Engineering at the ETH Zurich (Switzerland) where Dominik Werne, Thomas Jaggi, and Christoph Gisler supported the authors during testing. Ahmad Abo-El-Ezz performed the material tests on the masonry and bricks and assisted during the spandrel tests. All contributions are gratefully acknowledged.

REFERENCES

Bentz, E., 2001. *Response-2000, Shell-2000, Triax-2000, Membrane-2000 User Manual*, University of Toronto, Canada.

Beyer, K., Abo-El-Ezz, A., and Dazio, A., 2010a. *Quasi-Static Cyclic Tests on Different Types of Masonry Spandrels*, Report No. 327, Institute of Structural Engineering, ETH Zürich, Switzerland.

Beyer, K., Abo-El-Ezz, A., and Dazio, A., 2010b. Experimental investigation of the cyclic behaviour of unreinforced masonry spandrels, *Proc. of the 9th U.S. National and 10th Canadian Conference on Earthquake Engineering*, Toronto, Canada.

European Committee for Standardization (CEN), 2000. *EN 772-1: Methods of test for masonry units, Part 1: Determination of compressive strength*, European Committee for Standardization, Brussels, Belgium.

European Committee for Standardization (CEN), 2002. *EN 1052-1: Methods of test for masonry, Part 1: Determination of compressive strength*, European Committee for Standardization, Brussels, Belgium.

European Committee for Standardization (CEN), 2005. *EN 1998-3: Eurocode 8: Design of structures for earthquake resistance – Part 3: General rules, seismic actions and rules for buildings*, European Committee for Standardization, Brussels, Belgium.

European Committee for Standardization (CEN), 2006a. *EN 1015-11: Methods of test for mortar for masonry. Determination of flexural and compressive strength of hardened mortar*, European Committee for Standardization, Brussels, Belgium.

European Committee for Standardization (CEN), 2006b. *EN 12390-1: Steel for the reinforcement and prestressing of concrete – Test methods – Part 1: Reinforcing bars, wire rods and wire*, European Committee for Standardization, Brussels, Belgium.

European Committee for Standardization (CEN), 2007. *EN 1052-3: Methods of test for masonry – Part 3: Determination of initial shear strength*, European Committee for Standardization, Brussels, Belgium.

European Committee for Standardization (CEN), 2009a. *EN 12390-3: Testing hardened concrete – Part 3: compressive strength of test specimens*, European Committee for Standardization, Brussels, Belgium.

European Committee for Standardization (CEN), 2009b. *EN 12390-5: Testing hardened concrete – Part 5: Flexural strength of test specimens*, European Committee for Standardization, Brussels, Belgium.

Chen, W., 1970. Double punch test for tensile strength of concrete, *ACI Journal* **67**, 993–995.

Frumento, S., Magenes, G., Morandi, P., and Calvi, G.M., 2009. Interpretation of Experimental Shear Tests on clay brick masonry walls and evaluation of q-factors for seismic design, Technical Report 2009/02, IUSS Press, EUCENTRE and University of Pavia, Italy.

Gattesco, N., Clemente, I., Macorini, L., and Noè, S., 2008. Experimental investigation of the behavior of spandrels in ancient masonry buildings, *Proc. of the 14th World Conference on Earthquake Engineering*, Beijing, China.

Graziotti, F., Magenes, G., and Penna, A., 2009. Progetto di una sperimentazione su elementi di fascia muraria, *Rapporto Reluis, Allegato 4.3-UR01-1*, Università di Pavia e EUCENTRE, Pavia, Italy.

Magenes, G., and Della Fontana, A., 1998. Simplified non-linear seismic analysis of masonry buildings, *Proc. of the British Masonry Society*, No. 8, pp. 190–195.

Magenes, G., 2000. A method for pushover analysis in seismic assessment of masonry buildings, *Proc. of the 12th World Conference on Earthquake Engineering*, Auckland, New Zealand.

Milani, G., Beyer, K., and Dazio, A., 2009. Upper bound limit analysis of meso-mechanical spandrel models for the pushover analysis of 2-D masonry frames, *Engineering Structures* **31**, 2696–2710.

Ordinanza del Presidente del Consiglio dei Ministri (OPCM n. 343), 2005. Ulteriori modifiche ed integrazioni all'OPCM n. 3274 del 20 marzo 2003, recante „Primi elementi in materia di criteri generali per la classificazione sismica del territorio nazionale e di normative tecniche per le costruzioni in zona sismica, *Suppl. Ordinario n. 85 alla G.U. n. 107 del 10 maggio 2005*, Ordinanza del Presidente del Consiglio dei Ministri del 3 maggio 2005, Rome, Italy.

Priestley, M. J. N., Calvi, G. M., and Kowalsky, M. J., 2007. Displacement-based seismic design of structures, *IUSS Press*, Pavia, Italy.

Swiss Society of Engineers and Architects (SIA), 2003a. SIA262/1: Concrete – Supplementary Specifications. Building Code. Swiss Society of Engineers and Architects, Zürich, Switzerland.

Swiss Society of Engineers and Architects (SIA), 2003b. SIA266/1: Masonry – Supplementary Specifications. Building Code. Swiss Society of Engineers and Architects, Zürich, Switzerland.

(Received 1 February 2011; accepted 23 July 2011)